Computational Materials Science 137 (2017) 332–339

Contents lists available at ScienceDirect

Computational Materials Science

journal homepage: www.elsevier.com/locate/commatsci

Modulation effect on the effective mass of free carriers induced by multicomponent elements in In_2O_3-based transparent conducting oxides

Ying-Bo Lu [a,*], Haozhi Yang [b], Y.Q. Xin [a], Wei-Yan Cong [a]

[a] School of Space Science and Physics, Shandong University, Weihai 264209, China
[b] Supercomputing Center, Shandong University, Weihai 264209, China

ARTICLE INFO

Article history:
Received 25 March 2017
Received in revised form 1 May 2017
Accepted 5 June 2017
Available online 15 June 2017

Keywords:
Transparent conducting oxides
In_2O_3
Effective mass
Impurity codoping
Localization effect

ABSTRACT

Motivated by extensive investigations on the In_2O_3-based multicomponent transparent conducting oxides (TCOs), we want to know the carrier transport properties in these systems and how they evolve with adjusting of geometric structure and constituent elements. Guided by the empirical minimum effective mass physics, we select nine impurities M (M = Sn, Zn, Cd, Hg, Mn, Ni, Co, Ga and Ge) to tune the effective mass (m^*) of In_2O_3-based TCOs. By means of systematic theoretical investigations, we find that in impurity M isolated or corporately doped In_2O_3 materials, the substitutional position for dopant M is determined by the charge state. Codoping Sn and other eight impurities into In_2O_3 (to form IMTO) is an effective strategy to reduce the indium content in In_2O_3-based TCOs materials. For the recognized n-type carrier contributor, namely, V_O defect, it induce spatial localization and orbital localization effects in electronic structures and thus enlarge m^*, which are caused by the large lattice distortion and complicated orbital wavefunction hybridizations. However, for IMTO:V_O (M = Zn, Ga and Hg) systems, both localization effects are weakened, leading to a decrease of m^*. It even reduces by half value for In-Hg-Sn-O:V_O systems. This systematic work in In_2O_3-based materials may be helpful in designing of a new range of high performance TCOs.

1. Introduction

Owing to the high electric conductivity and transparency, transparent conducting oxides (TCOs) has wide applications in optoelectronics. A number of known and new TCOs are based on In_2O_3 materials. Until now, the most popular TCOs is indium tin oxide (ITO) with conductivities ranging from 103 S/cm to 4000 S/cm and transparencies over 90% in the visible spectrum [1]. However, because of the limited supply of indium (In) element, ITO becomes one of the most expensive components in many optoelectronic devices [2]. Combined with other drawbacks, ITO is hindered in the production of next generation large-scale flat panel display and photovoltaic technologies. This encourages us to search for low indium content alternative TCOs materials [3,4]. Recently, binary or ternary oxide systems, such as fluorine doped tin oxide, gallium-doped zinc oxide, aluminium-doped zinc oxide and zinc tin oxide etc., have been assessed as replacements for ITO [5,6]. At the same time, the performance of In_2O_3-based TCOs and its well-established processing parameters suggest that it is smart and convenient strategy to design new TCOs on the basis of In_2O_3 host crystal. Many dopants, e.g., Zn, Cd, Sn and Ga etc. [7–9], have been incorporated into In_2O_3 to tailor the electric and optical properties. The combination of these dopants with In_2O_3 provides a broad array of new TCOs materials [10,11]. For instance, In–Zn–Sn–O system was reported to have a resistivity ranging in 3–8 $\times 10^{-4}$ Ω·cm and an absorption edge of 2.9–3.65 eV. And most importantly, it reduces the indium content as low as 60 cation% [5,10,12–15].

It is realized that in essence, enhanced conductivity of n-type TCOs must be achieved via increasing the carrier mobility rather than increasing the carrier density [16]. Making TCOs with high mobility basically depends on two principles. The first one is mixing as many component oxides with distinctive crystal structures as possible to tailor the near band-edge structure. Secondly, *s*-orbitals of metal ions must be the main components of the bottom of conduction band (CB) [17]. Because the metal *s*-orbitals spatially spread with isotropic shape, and could overlap directly with neighbouring metal *s* orbitals [18], the *s*-like conduction band represents a uniform electronic charge density distribution and concomitant low scattering, which is beneficial to generate a low effective mass of free carriers (m^*). In opposite, compounds with large *d*-orbital character at the conduction band minimum (CBM) have much larger electronic effective mass [19–21]. So the position and the dis-

* Corresponding author.
E-mail address: lyb@sdu.edu.cn (Y.-B. Lu).

http://dx.doi.org/10.1016/j.commatsci.2017.06.005
0927-0256/

persion of the bottom of CB are most important features for the bandstructures of TCOs, which provides necessary evolution for the transparent conducting behaviours with electron doping. These principles tell us how to find a new material with effective masses (and mobility) close to that of the known n-type TCOs but performs better on additional application with specific properties (e.g., work function, cost or stability).

Impurity doping is proved as an effective method to modulate the physical properties of solid materials. Very low effective mass are observed in metal oxides making up with a region of metals between group 12 and group 15 in rows 4 and 5 (In, Sn, Zn, Cd, Ga, Ge and Sb), as well as for some transition metals (Mn, Co, and Ni), which show strong *s*-orbital character near CBM [22]. Therefore, careful engineering of the chemical constituents in In_2O_3-based systems containing those metal elements may render them useful materials for TCOs applications. For example, obvious increases in both carrier density and mobility in ZTO film were attributed to an enrichment of Sn [23]. In-Ga-Zn-O exhibits moderately high TFT mobility ($\sim$10 cm^2 V^{-1} s^{-1}) [5]. However, in these multicomponent (ternary or quaternary) compounds, the nature of these elements, the hybridization between tens of atomic orbitals and the contribution to the CBM from valence electron orbitals are complicated, so the detailed studies on their electronic band structures and accompanied properties have been limited. Particularly, detailed comparative studies in the theoretical aspects of the electronic structures and the geometric structures are still lacking, which play the key role in the reverse design of functional materials. Obtaining such understanding is the crucial step towards improvement of current materials and development of a new range TCOs with increased functionality and improved device performance [24].

Therefore, in this work, the detailed geometric structures and electronic structures of various impurity M (M = Sn, Zn, Cd, Hg, Mn, Ni, Co, Ga and Ge that may lead to potential small effective mass [22]) doping In_2O_3 materials are theoretically examined based on series of systematic ab initio calculations, especially for the case of Sn^{4+} codoping with other eight impurities. The relationship between local geometric structures, defects and effective mass in these series of TCOs materials is analysed elaborately.

2. Computation and simulation methods

In_2O_3 crystallizes in the bixbyite structure [25,26], in which In^{3+} ions occupy two crystallographically distinct sites, i.e., the b-sites (8 atoms, 25%) and the d-sites (24 atoms, 75%), respectively. At b-site, six In-O bonds are equidistant; while at d-site, there is a manifest distorted InO_6 octahedron, which are illustrated in Fig. 1 (b). When impurities are introduced into In_2O_3 supercell, the potential substitutional positions are labelled in Fig. 1(a).

All calculations are carried out using Vienna ab initio simulation package (VASP) [27,28]. The projector augmented wave (PAW) potential [29] is used to describe the electron-ion interactions, and the generalized gradient approximation (GGA) parameterized by Perdew-Burke-Ernzerhof (PBE) method [30] is used for electron exchange-correlation functional. A cutoff energy of 400 eV and a $3 \times 3 \times 3$ Monkhorst-Pack k-grid are used to integrate wavefunctions in the first Brillouin zone. All atomic positions and lattice parameters are relaxed until the residual atomic forces are smaller than 0.01 eV/Å. The self-consistent convergence threshold is set to 10^{-6} eV. In our GGA+U calculations [31], the effective interaction parameters U-J are set to 7.5 eV for 3*d*-orbitals of Zn and 7.0 eV for n*d*-orbitals of M (M=In, Sn, Hg, Cd, Mn, Ni, Co, Ga and Ge), respectively [32–34].

3. Results and discussions

3.1. Geometry structures

When these selected nine elements are doped into In_2O_3 lattice isolated or corporately, they all tend to substitute the host cations. Because of their different radii or/and valence electrons comparing with host indium atoms, the spatial distributions of defects/associates and thus the geometric structures of doped In_2O_3 systems show diverse performance, making In_2O_3-based materials exhibit complicated and changeful physical properties. Actually, this is why we use the doping strategy to modulate the electronic properties of In_2O_3-based TCOs materials. We use formation energy to represent the difficulty of doping these impurities into In_2O_3, and the calculation methods are presented in supplementary materials. By analyses of formation energies for each configuration of impurity doped In_2O_3 materials, we obtain the favourite geometric structure for each impurity in In_2O_3.

Once it is reported that a dopant cation smaller than the host lattice cation prefers to occupy the d-site, while a dopant cation larger than the host cation tends to locate at the b-site in bixbyite sesquioxide [35,36]. The ionic radii of In^{3+}, Sn^{4+}, Zn^{2+}, Cd^{2+}, Hg^{2+}, Mn^{2+}, Ni^{2+}, Co^{3+}, Ga^{3+} and Ge^{4+} are 0.80, 0.69, 0.74, 0.95, 1.02, 0.82, 0.69, 0.75, 0.62 and 0.53 Å, respectively. If the reported rule

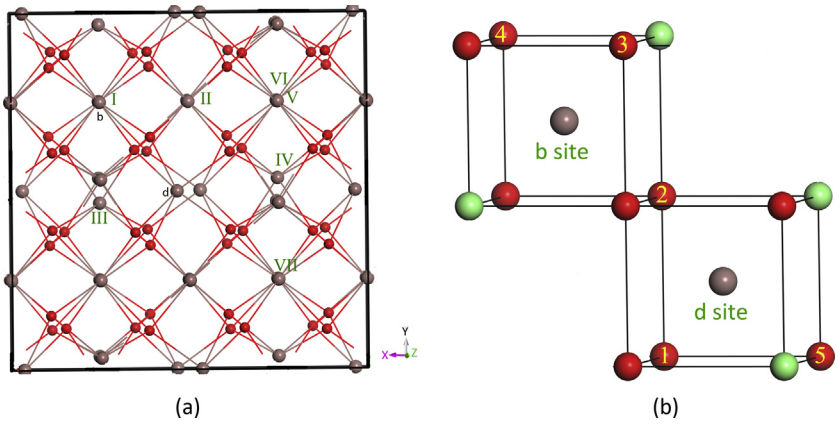

Fig. 1. (a) The geometry structure of bixbyite In_2O_3 crystal. (b) The schematic plot of the cation-oxygen octahedrons in bixbyite structure, with cations locating at b-site and d-site, respectively. The red and ocherous balls represent the oxygen and indium atoms, respectively. The green balls represent the structural vacancies. The Roman numerals I–VII in (a) denote positions of substitutional dopant and the Arabic numerals 1–5 in (b) denote positions of V_O defects in various defective configurations. (For interpretation of the references to color in this figure legend, the reader is referred to the web version of this article.)

remains to work, the substitutional defects Sn_{In}, Zn_{In}, Ni_{In}, Co_{In}, Ga_{In} and Ge_{In} should locate at the d-site in In_2O_3 lattice, whereas Cd_{In}, Hg_{In} and Mn_{In} defects lie in b-site. However, our calculated results disagree with that anticipation. We find that Zn_{In}, Cd_{In}, Hg_{In}, Mn_{In} and Ni_{In} defects locate at d-site, while Sn_{In}, Co_{In}, Ga_{In} and Ge_{In} occupy the b-site, which is deduced form the comparison between energies of all considered dopants at different positions (i.e., b-site and d-site) elaborately in Table S1 in the supplementary materials. Hence it comes to a conclusion that a divalent ion prefers to substitute the d-site In^{3+}, but a trivalent/tetravalent ion favors the b-site. We attribute this phenomenon to the valence electrons (charge states) difference between host indium ion and impurity ions. When impurity M ion is divalent, such as Zn^{2+} and Hg^{2+} etc., the different valence electrons between M^{2+} and In^{3+} ions give birth to a large lattice distortion around M^{2+} and destroy the symmetry of local geometric structure. As discussed above, the symmetry around d-site In^{3+} ion is low (point group: C_2) originally, so it is more suitable to accommodate the large lattice distortion induced by M^{2+} substitutional defect than the b-site lattice position. However, when dopant goes to be Co^{3+} and Ga^{3+}, they are trivalent impurities, just as that of indium host cation. The isovalent substitutions of Co_{In} and Ga_{In} yield weak lattice distortion and tend to occupy the high symmetric position, namely, b-site position. For tetravalent impurity ions, i.e., Ge^{4+}/Sn^{4+}, they donate one more valence electron than In^{3+}, but the free-electron-like wavefunctions are too dispersive to make this extra valence electron localize around the impurity position. Therefore, the lattice distortion induced by tetravalent ions resemble that produced by trivalent impurities, then they also favor the more symmetric b-site position in In_2O_3 lattice. Fig. 2 illustrates this suggestion in more intuitionistic view by plots of charge density differences, where we take Zn^{2+}, Ga^{3+} and Sn^{4+} doped In_2O_3 for example. The charge density differences induced by Zn^{2+} and Ga^{3+} predominantly localize in the area near themselves, but the excess electron provided by Sn^{4+} dopant distributes throughout the whole supercell.

As there are extensive investigations on Sn^{4+} and other cations codoping In_2O_3 materials [37–44], we also codope Sn and other eight metals into In_2O_3 lattice to form IMTO (M = Zn, Cd, Hg, Mn, Ni, Co, Ga and Ge) quaternary compounds and explore their formation energies and geometric structures. For each of these IMTO materials, we employ three configurations to simulate the random distributions of M and Sn impurities in the whole In_2O_3 lattice, and to search for the most stable one. In all configurations, as marked in Fig. 1(a), Sn is always fixed at position I, while M atoms are located at different sites (being labelled with Roman numerals II∼VII) to represent configurations with different distances between Sn and M dopants. By plenty of calculations, we find that in IMTO (M = Zn, Cd, Hg, Mn and Ni) materials, Zn, Cd, Hg, Mn and Ni tend to occupy d-site and Sn stays in the b-site, which is already indicated by conclusions from the isolated M-doped In_2O_3 systems. Meanwhile, judged from formation energies listed in Table S1 in supplementary materials, MO_6 octahedrons around impurities

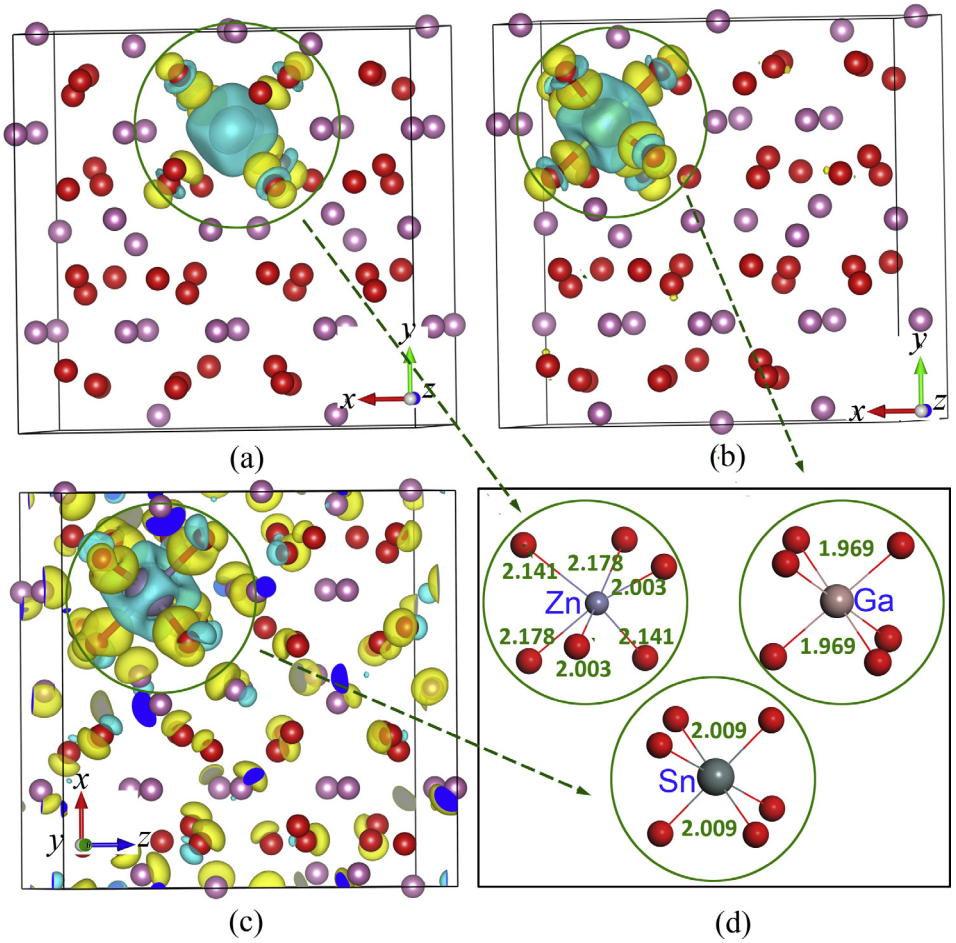

Fig. 2. Charge density differences of (a) Zn-doped, (b) Ga-doped and (c) Sn-doped In_2O_3 supercells. (d) shows the local structures around Zn, Ga and Sn dopants in these three impurity doped In_2O_3 materials. The numbers in (d) denote the bond lengths of M-O bonds (M = Zn, Ga and Sn), respectively. The yellow and blue isosurfaces represent the increase and the decrease in the total charge density, respectively. (For interpretation of the references to color in this figure legend, the reader is referred to the web version of this article.)

Table 1
The formation energies (under O-rich limit and In-rich limit) of stoichiometric In_2O_3, single M (M = Sn, Zn, Hg, Cd, Mn, Ni, Co, Ga and Ge) doped In_2O_3, the M/Sn codoped In_2O_3 (namely, IMTO) with and without V_O defect, respectively. For each case, we present the results of the most energetic stable configuration.

System	Formation energy (eV)	
	O-rich	In-rich
In_2O_3	−11.534	
In_2O_3:Sn	2.282	0.342
In_2O_3:Zn	1.439	3.376
In_2O_3:Cd	0.967	2.904
In_2O_3:Hg	−1.867	0.070
In_2O_3:Mn	−2.698	−0.761
In_2O_3:Ni	−0.14	1.797
In_2O_3:Co	−1.65	0.287
In_2O_3:Ga	0.801	0.801
In_2O_3:Ge	1.336	−0.602
In-Zn-Sn-O	0.942	0.941
In-Cd-Sn-O	0.545	0.544
In-Hg-Sn-O	−1.976	−1.977
In-Mn-Sn-O	−0.404	−0.405
In-Ni-Sn-O	−0.207	−0.208
In-Co-Sn-O	0.494	0.493
In-Ga-Sn-O	3.013	1.075
In-Ge-Sn-O	5.754	1.878
In_2O_3:V_O	5.201	1.350
In-Zn-Sn-O:V_O	5.838	1.962
In-Cd-Sn-O:V_O	5.292	1.416
In-Hg-Sn-O:V_O	1.683	−2.193
In-Ni-Sn-O:V_O	4.687	0.811
In-Co-Sn-O:V_O	4.883	1.007
In-Ga-Sn-O:V_O	8.325	2.512
In-Ge-Sn-O:V_O	11.314	3.563

(Zn, Cd, Hg, and Ni) tend to be nearest neighbouring to SnO_6 octahedron, just as illustrated in Fig. 1(b), which is ascribed to the isovalent substitution of two In^{3+} ions with one Sn^{4+} and one M^{2+} ions together. This isovalent codoping effect is already discussed elaborately in our previous studies [20]. When tetra/tri-valent impurities (i.e., Co^{3+}, Ga^{3+}, Ge^{4+}) and Sn^{4+} are codoped into In_2O_3, all these impurities and Sn^{4+} atoms tend to substitute the b-site indium atoms. These phenomena are also in accord to conclusions obtained from impurity isolated doped In_2O_3 system. Nevertheless, the MO_6 octahedrons for M = Co^{3+}, Ga^{3+}, Ge^{4+} prefer to be far away from SnO_6 octahedron, for the generation of repulsive forces between positive charge centres (Sn^{4+} and/or Ge^{4+}) that are uncompensated by other dopants. For each of those dopants, the formation energy of the most stable configurations is listed in Table 1, from where we find that among these nine impurities, formation energies of isolated doping In_2O_3 with Hg, Mn, Ni and Co impurities are relative smaller than others. When Sn and other M dopants cooperate to form IMTO, the formation energies of M = Hg, Mn, Ni and Co are also small, indicating the easier formation of these quaternary compounds and the concentration of impurities can reach a large value, this is confirmed by lots of previous researches. But there's no exact definition on how many impurities can make the host lattice to be an alloy, and this question is beyond our research scope in this paper and should be studied further.

There is another interesting phenomenon we should take into account, i.e., how does the oxygen deficient defect (V_O) work in these doped systems. Because it is proposed extensively in previous investigations that in In_2O_3-based materials, V_O defect is the dominant origin to generate the free carriers accounting for the experimentally observed n-type conductivity. So we turn to study the V_O including quaternary IMTO (IMTO:V_O) system. For each of these eight M/Sn codoped In_2O_3 materials, we construct six configurations to examine the favourite position of V_O, in which the positions of V_O are signalled in Fig. 1(b) with numbers of 1–5 plus one position that far away from M/Sn dopant pairs (not shown in Fig. 1). The calculated results reveal that no matter which dopant M is codoped into In_2O_3 lattice with Sn dopant, V_O always tends to exist in MO_6 octahedron, not in SnO_6 octahedron. we believe that due to the high symmetric local structure in SnO_6 octahedron

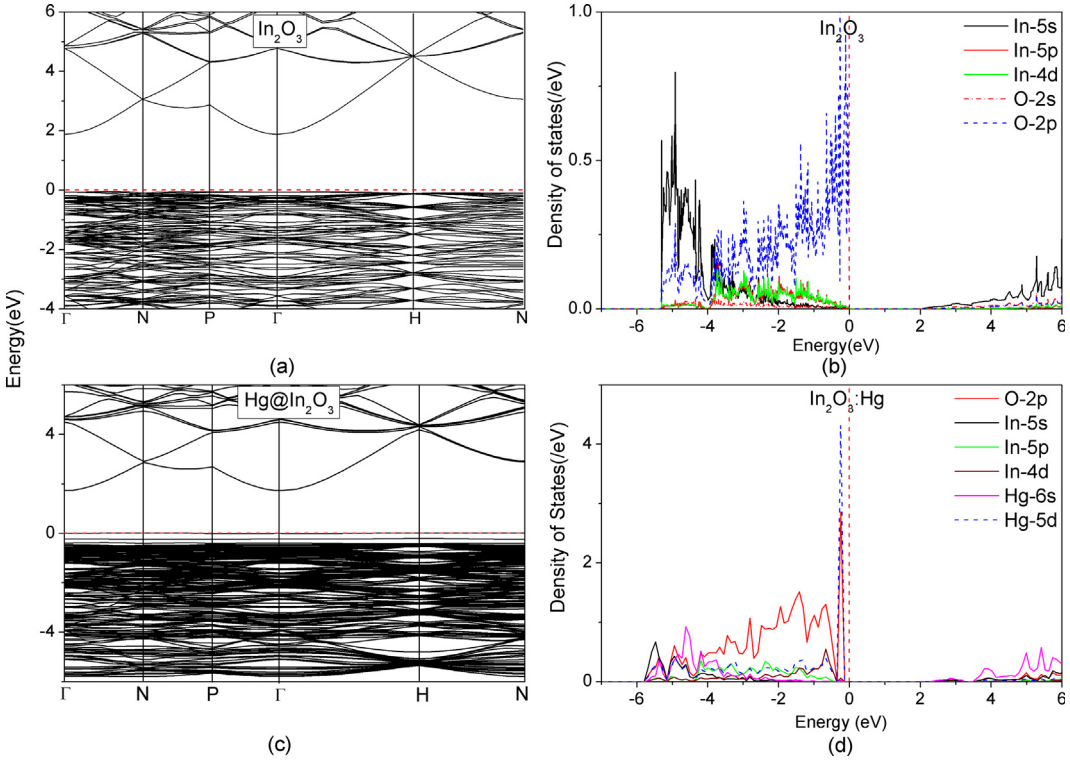

Fig. 3. (a) The bandstructure and (b) PDOS of In_2O_3, respectively. (c) The bandstructure and (d) PDOS of In_2O_3:Hg crystals, respectively. The red dashed lines in these plots represent Fermi level.

and the strong cohesive energy of Sn-O coordination, Sn-O bond is hard to be broke and thus V_O is difficult to form in SnO_6 octahedron [20].

From Table 1 we can see that the inclusion of V_O defect in In_2O_3 systems leads to the increase of formation energy, originating from the local structure reconstruction around the oxygen defect destroys the periodic crystalline structure. However, when V_O is introduced into IMTO systems, the formation energy changes variously. For example, for IMTO:V_O systems (M = Zn, Cd, Ni and Co), the formation energy changes little. While for the tetra/trivalent dopant, the formation energy of IMTO:V_O system (M = Ga and Ge) increases manifestly. This is because that the incorporation of V_O into IMTO (M = Ga and Ge) systems give rise to strong local lattice distortion around the tetra/trivalent dopant, as shown in Fig. 4(d). However, IMTO:V_O systems (M = Zn, Cd, Ni and Co) reserve almost the same local geometric structure as that in In_2O_3:V_O systems, so the formation energies have the similar value. In-Hg-Sn-O system is an exception, in which the formation energy of V_O decreases obviously. From Fig. 4(b) we can see that Hg atom moves off the centre of original HgO_6 octahedron and partially compensates the vacant induced by V_O, so the lattice distortion induced by V_O are released partially and thus the formation energy of V_O becomes a smaller value.

3.2. Electronic structures of IMTO solutions

As pointed out in the introduction section, our main research interest is to explore how these various dopants M can affect the electronic and transport properties of In_2O_3 and to find if there are some quaternary oxides with intrinsic/extrinsic defects showing promising applications as good TCOs materials. The bandstructure is one of the most important profiles to represent the electronic properties. The bandstructure of perfect In_2O_3 crystal is plotted in Fig. 3(a) with an indirect band gap of 1.92 eV. Density of states (DOS) of bixbyite In_2O_3 in Fig. 3(b) shows that the bonding and nonbonding O-2*p* states predominantly form the valence band (VB), while conduction band is comprised of the antibonding state yielded by strong In-5*s*/O-2*p* interactions. It is already proposed that the lowest effective mass chemistries are correlated with a strong *s*-orbital character in CBM. So the effective mass m^* of In_2O_3 is low, arising from In-5*s*/O-2*p* overlap near CBM.

When In_2O_3 is doped with isolated M or is codoped with M/Sn pair to construct ternary or quaternary compound, bandstructures change little. Most of these materials have band gaps ranging in [1.90 eV, 2.1 eV], which are the almost same value of pure In_2O_3, except that Hg doped In_2O_3 (In_2O_3:Hg) system or Hg/Sn codoped In_2O_3 (In-Hg-Sn-O) system have the obvious smaller band gaps, as shown in Fig. 3(c). For more detailed descriptions, we can review all bandstructures of M-doped or M/Sn-codoped In_2O_3 materials that are illustrated in supplementary materials. Considering the underestimated band gap of GGA function we used, most of these multicomponent semiconductors are still transparent in the visible spectrum.

The dispersion of CBM provides one of the key parameters to represent the transport properties of TCOs, namely, the effective mass of free carriers. For all of these nine elements singly doped

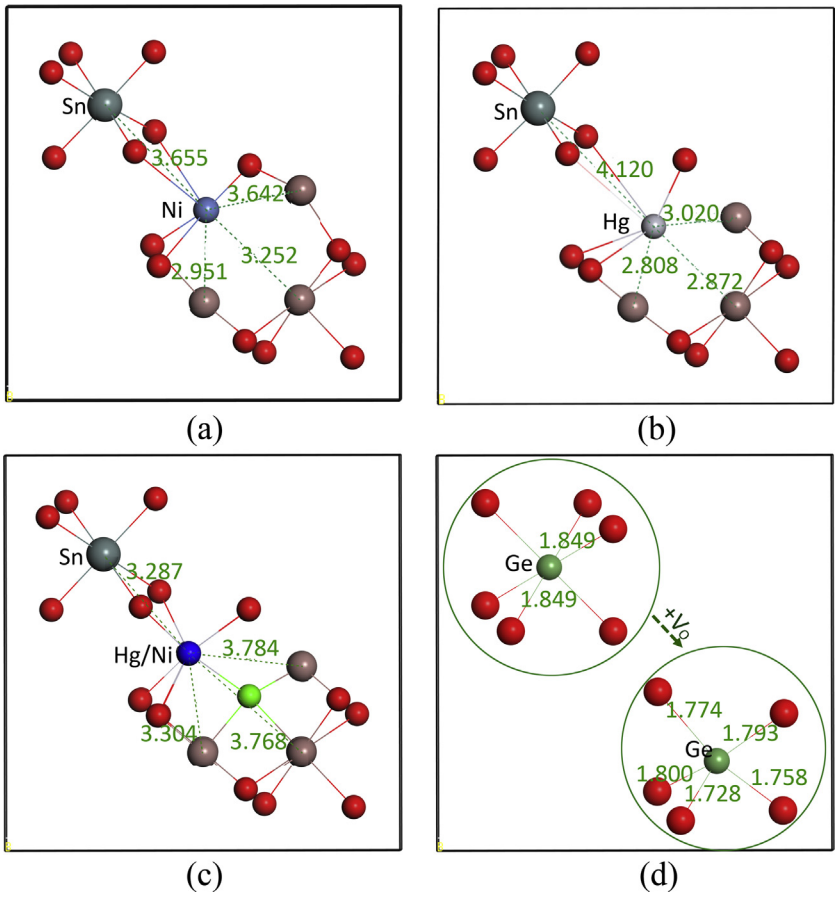

Fig. 4. Local structures around V_O defect in (a) In-Ni-Sn-O:V_O system, (b) In-Hg-Sn-O:V_O system, (c) unrelaxed IMTO:V_O systems and (d) In-Ge-Sn-V_O system. In these plots, the red and ocherous balls represent the oxygen and indium atoms, respectively. Positions of dopant are marked in these plots accordingly. The blue and green balls in (c) represent the M (M = Hg or Ni) and V_O defect, respectively. (d) illustrate the GeO_6 octahedron without V_O defect (top left) and with V_O defect (bottom right). (For interpretation of the references to color in this figure legend, the reader is referred to the web version of this article.)

or codoped In_2O_3 systems with most energetic stable configurations, all their effective mass of free carriers are calculated and are listed in Table 2. These data reveal that the effective masses m^* of pure In_2O_3 along three different directions in the reciprocal space are almost the same value, around 0.190 m_e. These m^* are low enough to ensure the good transport properties for free electrons in In_2O_3. As stated above, we want to tune (actually, we want to decrease) m^* by means of impurity singly doping or codoping method. However, m^* listed in Table 2 show that neither M singly doping nor M/Sn codoping could reduce the effective mass in an obvious way, and in the reverse, most of them are enlarged with a minor value, due to the bandstructure renormalization effect generated by complicated many-body interactions. The increase of m^* induced by impurity in semiconductors is similar as the case in previous reports [45], where m^* increases from 3.7 m_e to 5.6 m_e with materials going from Cu_2O to Cu_3VO_4.

3.3. Electronic structures of IMTO with V_O defects

More interesting phenomena emerge when we inspect the effective mass of these materials with V_O defect. V_O breaks the periodic crystalline structure and brings manifest disturbance to the electronic wavefunctions of nearest neighbouring (NN) indium atoms or next nearest neighbouring (NNN) O atoms. This changes the bandstructure near CBM and increases the effective mass m^* from 0.190 m_e to 0.851 m_e along Γ-H direction in the reciprocal space, which can be found in Table 2. When system is changed to IMTO:V_O, m^* change in different ways. For IMTO (M = Zn, Ga and Hg) with V_O systems, m^* decrease to smaller values, especially reduces by half value for In-Hg-Sn-O system, in comparison with In_2O_3:V_O. This means that for V_O containing In_2O_3 systems, the transport ability may be promoted greatly by Hg/Sn codoping. However, m^* increase with a large factor for IMTO:V_O (M = Mn, Co, Ni). For instance, In-Ni-Sn-O:V_O system has a very large m^* of 8.920 m_e along Γ-P direction, which is disadvantaged for electrons transport in In_2O_3 host crystalline. For IMTO (M = Ge and Cd) including V_O materials, their effective masses are intervening values between those two cases just mentioned. The origin of the distinct performances of these quaternary compounds can be interpreted by deep analyses from PDOS. In principle, the transport paths in crystalline lattice are constructed by the spatial overlap and the energetic overlap between those extended wavefunctions of constituent elements, which are illustrated by PDOS of the specific systems. It is proposed that if CBM of one system is contributed predominantly by the nonlocalized and directionless cation-*s* orbitals, the bottom of CB would be dispersive and give birth to a low m^*. However, wavefunctions of *p*/*d* orbitals show evident directionality, which make the bonding direction between cation and anion atoms (that is, the charge transport path) anisotropic. So if *p*/*d* orbitals contribute considerably to the bottom of CB, m^* may exist in a large value [46]. Therefore, we take three specific samples, i.e., In-Hg-Sn-O solution, In-Ni-Sn-O solution and In-Ge-Sn-O solution, to represent the three variation tendency of m^* (decreased, increased and unchanged) in IMTO:V_O materials, respectively. Contributions to CBM from various atomic orbitals in these three systems are calculated and listed in Table 3.

The calculated data show that the bottom of CB originates primarily from the hybridization between *s*-orbital of cation and *p*-orbital of oxygen atoms. The anisotropic filled *d* shell does not typically take part in TCOs bonding. Clearly, the *sp* hybridization provides the relative uniform charge distribution within the In_2O_3 cell, constructing a three dimensional In-5*s*/O-2*p* network for charge transport once extra carriers are conducted, e.g., by V_O. However, if a V_O defect is actually generated in In_2O_3 lattice, the bottom of CB of In_2O_3 changes evidently. Firstly, contributions from NN indium and NNN oxygen atoms increase to 5.50 and 1.50 times of the original values in perfect In_2O_3 lattice, respectively. Secondly, contributions from *p*/*d* orbitals are reinforced, especially for NN indium atoms. Comparing with pure In_2O_3 materials, contributions from In-5*p* and 4*d* orbitals increase with a factor of 6 and 3 times, respectively. Above all, two localization effects, or we name them as "spatial localization" and "orbital localization" effects, respectively, weaken the charge transport ability in In_2O_3:V_O material.

When V_O is introduced into Ge/Sn codoped In_2O_3 (In-Ge-Sn-O:V_O) materials, electronic structure near CBM changes little, the *spatial localization* and *orbital localization* effects around V_O defect are reserved. Contribution from Sn atom resembles that of indium host atom far away from these defects. Contribution from *s*-orbital of Ge decreases, and in the other hand, *p*/*d*-orbitals of Ge provide more contributions to CBM. But these variations are not large enough to change the character of CBM and m^* of In-Ge-Sn-O:V_O systems in a manifest magnitude. When V_O is introduced into transitional metals and Sn codoping In_2O_3, such as In-Ni-Sn-O solutions, both *spatial localization* and *orbital localization* effects of NN indium element or NNN O element induced by V_O retain the similar performances as in pure In_2O_3:V_O system, and do not change much. However, as mentioned in the first paragraph in this section, V_O defect tends to exist in NiO_6 octahedron. Ni dopant locates at the d-site in bixbyite structure, so the local geometric symmetry around Ni is worse than that of other cations in b-site. Meanwhile, the introduction of V_O worsens the symmetric structure in NiO_6 octahedron further. Nevertheless, the partial filled Ni-3*d* orbital is active to chemical reaction and takes part in the bonding inter-

Table 2
Effective masses of free carriers for these nine dopant M single doped or codoped In_2O_3 materials. The Configurations of M/Sn codoped In_2O_3 materials with V_O defect (IMTO:V_O) are also considered.

Configuration		Effective mass (m_e)			Configuration		Effective mass (m_e)		
M	Defects	Γ-H	Γ-N	Γ-P	M	Defects	Γ-H	Γ-N	Γ-P
Zn	In_2O_3:Zn	0.199	0.201	0.203	Cd	In_2O_3:Cd	0.200	0.199	0.199
	In-Zn-Sn-O	0.203	0.204	0.204		In-Cd-Sn-O	0.198	0.200	0.198
	In-Zn-Sn-O:V_O	0.738	0.624	0.782		In-Cd-Sn-O:V_O	1.003	1.106	0.904
Mn	In_2O_3:Mn	0.211	0.208	0.221	Hg	In_2O_3:Hg	0.199	0.198	0.201
	In-Mn-Sn-O	0.202	0.166	0.203		In-Hg-Sn-O	0.206	0.207	0.203
	In-Mn-Sn-O:V_O	9.381	4.403	3.544		In-Hg-Sn-O:V_O	0.453	0.467	0.468
Ni	In_2O_3:Ni	0.203	0.201	0.201	Co	In_2O_3:Co	0.205	0.205	0.206
	In-Ni-Sn-O	0.203	0.196	0.198		In-Co-Sn-O	0.207	0.208	0.203
	In-Ni-Sn-O:V_O	6.868	2.525	8.920		In-Co-Sn-O:V_O	1.245	2.290	2.196
Ga	In_2O_3:Ga	0.200	0.199	0.198	Ge	In_2O_3:Ge	0.193	0.195	0.192
	In-Ga-Sn-O	0.200	0.202	0.199		In-Ge-Sn-O	0.199	0.205	0.205
	In-Ga-Sn-O:V_O	0.742	0.813	0.693		In-Ge-Sn-O:V_O	0.872	0.845	0.829
–	In_2O_3	0.190	0.181	0.190					
	In_2O_3:V_O	0.851	0.882	0.804					

Table 3
Contributions to the bottom of conduction band, which are projected on constituent elements in In_2O_3-based TCOs with V_O defect. In the first row, O(1), O(2), O(3), In(1) and In(2) denote contributions from oxygen and indium atoms, where the distance between them and the induced defect increases from near to far, respectively. "M" represents the impurities Zn, Cd, Hg, Mn, Ni, Co, Ga and Ge, respectively. The phrase "total" in the second column represents the total contributions summed over a specific atom, and are in units of eV. The characters, *s*, *p*, *d* in the second column, represent the corresponding atomic orbital contribution ratio of total contributions.

Configuration	Orbitals	O(1)	O(2)	O(3)	In(1)	In(2)	Sn	M
In_2O_3	*s*	46.67%	–	–	84.00%	–	–	–
	p	53.33%	–	–	8.00%	–	–	–
	d	–	–	–	8.00%	–	–	–
	Total	0.015	–	–	0.024	–	–	–
In_2O_3:V_O	*s*	14.29%	41.67%	50.00%	23.38%	76.00%	–	–
	p	85.71%	58.33%	50.00%	49.35%	12.00%	–	–
	d	–	–	–	27.27%	12.00%	–	–
	Total	0.021	0.012	0.012	0.077	0.025	–	–
IMTO:V_O (M = Hg)	*s*	30.77%	57.14%	50.00%	39.02%	73.91%	78.95%	39.02%
	p	69.23%	42.86%	50.00%	34.15%	13.04%	10.53%	50.00%
	d	–	–	–	26.83%	13.04%	10.53%	10.98%
	Total	0.013	0.014	0.012	0.041	0.023	0.019	0.082
IMTO:V_O (M = Ge)	*s*	42.86%	53.33%	46.15%	20.25%	77.42%	83.33%	57.14%
	p	57.14%	46.67%	53.85%	55.70%	9.68%	5.56%	19.05%
	d	–	–	–	24.05%	12.90%	11.11%	23.81%
	Total	0.014	0.015	0.013	0.079	0.031	0.018	0.021
IMTO:V_O (M = Ni)	*s*	41.67%	54.55%	53.85%	22.22%	80.00%	75.00%	2.17%
	p	58.33%	45.45%	46.15%	49.38%	10.00%	12.50%	21.74%
	d	–	–	–	28.40%	10.00%	12.50%	76.09%
	Total	0.012	0.011	0.013	0.081	0.020	0.016	0.092

action during the preparation of In-Ni-Sn-O systems with V_O defect. All these factors lead the orbital hybridizations between Ni and neighboring indium/oxygen atoms to a complicated one. As shown in Table 3, among contributions of Ni elements to the bottom of CB, 76.09% of which is provided by Ni-3*d* orbital, while Ni-4*s* orbital offers only 2.17%. Wavefunctions of *d*-orbital is direction dependent and of localized nature, it hinders the electron transport in lattice and thus the effective mass of In-Ni-Sn-O:V_O system is enlarged to 10 times of the value in In_2O_3:V_O, just as depicted in Table 2.

In comparison with In_2O_3:V_O materials, m^* of In-Hg-Sn-O system with V_O defect (In-Hg-Sn-O:V_O) reduces nearly 50%, profiting from the lessening of both *spatial localization* and *orbital localization* effects on wavefunctions around V_O defect. Firstly, in In_2O_3:V_O system, contributions to bottom of CB from NN indium and NNN oxygen (In(1) and O(1) in Table 3) around V_O are 0.077 and 0.021, respectively, which are 3.08 and 1.75 times of values from In and O atoms far away from V_O defect (denoted as In(2) and O(3) in Table 3), respectively. However, in In-Hg-Sn-O:V_O systems, contributions to the bottom of CB from NN indium and NNN oxygen (In(1) and O(1) in Table 3) around V_O are 0.041 and 0.013, respectively, which are 1.78 and 1.08 times of values from In and O far away from V_O defect, respectively. This means the disturbance induced by V_O defect on wavefunctions of atoms around V_O is weakened, leading to a lesser spatial localization effect around V_O. Secondly, from Table 3 we can see that contribution ratios to the bottom of CB from *s*-orbitals of NN indium and NNN oxygen around V_O in In_2O_3:V_O are 23.38% and 14.29%, respectively, which are much smaller than contribution ratios from *p*- and *d*-orbitals. Whereas in In-Hg-Sn-O:V_O systems, contribution ratio from *s*-orbital increases to 30.77% for NNN O around V_O defect. And for NN indium atoms, contribution ratio from *s*-orbitals even increases to 39.02%, a larger value than that from *p*/*d*-orbitals. The weakening of both *spatial localization* and *orbital localization* effects are beneficial to the electron transport throughout the whole lattice space, giving birth to a lower effective mass of about 0.46 m_e, almost the half value of In_2O_3:V_O system.

Compared to Ni/Sn codoping In_2O_3:V_O materials, when Hg and Sn are codoped into In_2O_3:V_O, Hg atom moves off the centre of original HgO_6 octahedron and partially compensates the vacant induced by V_O, as illustrated in Fig. 4. Hg atom is closer to indium atoms that originally bond to the lost O atoms. For example, the distances between Hg and these indium atoms decrease from 3.78Å to 3.02Å. The atomic orbital overlap integral can be affected by the distance between the nearest neighbours of metal ions. Considering the larger radius and the more dispersive wavefunctions projecting on 6*s* orbitals of Hg element, the closer distance between Hg and In atoms makes Hg and In atoms re-bond. Although the rebonding interaction is still weak, it is sufficient to lessen the orbital localization induced by V_O defect. The weakening of both spatial localization and orbital localization effects also means the transport paths for free electrons are re-building and thus the effective masses of free carriers are reduced, being proved by data in Table 2.

4. Conclusions

By means of systematic theoretical investigations, we study the detailed transport properties of various impurity M (M= Sn, Zn, Cd, Hg, Mn, Ni, Co, Ga and Ge) doped In_2O_3 materials that may possess potential low effective mass, and examine the relations between geometric structures and these electronic properties. We find that:

(1). In M is singly or corporately doped In_2O_3 materials, Zn, Cd, Hg, Mn and Ni locate at d-site, while Sn, Co, Ga and Ge occupy the b-site in bixbyite structures. The substitutional positions are determined by charge states.
(2). Codoping Sn and other eight impurities into In_2O_3 is an effective strategy to reduce the indium content in In_2O_3-based TCOs materials.
(3). As the well-known n-type carrier contributor, V_O defect destroys the electron transport path and increases the effective mass of free carriers, represented by the ***spatial localization*** and ***orbital localization*** effects in detailed electronic structures.
(4). When Sn and M dopants are codoped into In_2O_3:V_O to form IMTO:V_O systems, the *spatial localization* and *orbital localization* effects evolve in different tendencies. For IMTO:V_O (M= Zn, Ga and Hg) systems, both localization effects are weakened, so m^* decrease. It even reduces by half value for In-Hg-Sn-O:V_O system. This means that for V_O containing In_2O_3 systems, the transport ability may be promoted greatly by Hg/Sn codoping.

Obtaining such systematic understanding for In_2O_3-based materials is helpful. By careful engineering of these constituent elements in In_2O_3-based materials, for example, employing IMTO (M = Zn, Ga and Hg) systems (especially In-Hg-Sn-O systems), we can improve the current materials and develop a new range of high performance TCOs.

Acknowledgments

This work is supported by the National Natural Science Foundation of China under Grant 11504202. The calculations in this work were carried out on the supercomputing system in the Supercomputing Center of Shandong University, Weihai.

Appendix A. Supplementary material

Supplementary data associated with this article can be found, in the online version, at http://dx.doi.org/10.1016/j.commatsci.2017.06.005.

References

[1] Damisih, H.C. Ma, J.-J. Kim, H.Y. Lee, The electrical and optical properties of indium zinc tin oxide thin films with different Sn/Zn ratio, Thin Solid Films 520 (2012) 3741–3745.
[2] F. Bonaccorso, L. Colombo, G. Yu, M. Stoller, V. Tozzini, A.C. Ferrari, R.S. Ruoff, V. Pellegrini, Graphene, related two-dimensional crystals, and hybrid systems for energy conversion and storage, Science 347 (2015) 1246501.
[3] D.E. Proffit, S.P. Harvey, A. Klein, R. Schafranek, J.D. Emery, D.B. Buchholz, R.P.H. Chang, M.J. Bedzyk, T.O. Mason, Surface studies of crystalline and amorphous Zn–In–Sn–O transparent conducting oxides, Thin Solid Films 520 (2012) 5633–5639.
[4] S.H. Kwon, J.H. Jung, W.S. Cheong, G.H. Lee, P.K. Song, Dependence of electrical and mechanical durability on Zn content and heat treatment for co-sputtered ITZO films, Curr. Appl. Phys. 12 (2012) S59–S63.
[5] M.-G. Kim, H.S. Kim, Y.-G. Ha, J. He, M.G. Kanatzidis, A. Facchetti, T.J. Marks, High-performance solution-processed amorphous zinc−indium−tin oxide thin-film transistors, J. Am. Chem. Soc. 132 (2010) 10352–10364.
[6] J. Lee, D.-Y. Cho, J. Jung, U. Ki Kim, S. Ho Rha, C. Seong Hwang, J.-H. Choi, Theoretical and experimental studies on the electronic structure of crystalline and amorphous ZnSnO3 thin films, Appl. Phys. Lett. 102 (2013) 242111.
[7] S.W. Heo, Y.D. Ko, Y.S. Kim, D.K. Moon, Enhanced performance in polymer light emitting diodes using an indium-zinc-tin oxide transparent anode by the controlling of oxygen partial pressure at room temperature, J. Mater. Chem. C 1 (2013) 7009–7019.
[8] D.-J. Lee, J.-Y. Kwon, J. Kim, K.-J. Kim, Y.-H. Cho, S.-Y. Cho, S.-H. Kim, J. Xu, K.-B. Kim, Ultrasmooth, high electron mobility amorphous In–Zn–O films grown by atomic layer deposition, J. Phys. Chem. C 118 (2014) 408–415.
[9] K.J. Chen, F.Y. Hung, S.J. Chang, S.J. Young, Z.S. Hu, S.P. Chang, An investigation of the microstructure, optical and electrical properties of ZITO thin film using the sol–gel method, J. Sol-Gel Sci. Technol. 54 (2010) 347–354.
[10] J. Ni, H. Yan, A. Wang, Y. Yang, C.L. Stern, A.W. Metz, S. Jin, L. Wang, T.J. Marks, J. R. Ireland, C.R. Kannewurf, MOCVD-derived highly transparent, conductive zinc- and tin-doped indium oxide thin films: precursor synthesis, metastable phase film growth and characterization, and application as anodes in polymer light-emitting diodes, J. Am. Chem. Soc. 127 (2005) 5613–5624.
[11] C.A. Hoel, J.M.G. Amores, E. Moran, M.A. Alario-Franco, J.-F.O. Gaillard, K.R. Poeppelmeier, High-pressure synthesis and local structure of corundum-type In2-2xZnxSnxO3 (x e 0.7), J. Am. Chem. Soc. 132 (2010) 16479–16487.
[12] C.W. Ow-Yang, H.-Y. Yeom, D.C. Paine, Fabrication of transparent conducting amorphous Zn–Sn–In–O thin films by direct current magnetron sputtering, Thin Solid Films 516 (2008) 3105–3111.
[13] A. Ambrosini, S. Malo, K.R. Poeppelmeier, M.A. Lane, C.R. Kannewurf, T.O. Mason, Zinc doping in cosubstituted In2-2xSnxZnxO3-δ, Chem. Mater. 14 (2002) 58–63.
[14] C.A. Hoel, D.B. Buchholz, R.P.H. Chang, K.R. Poeppelmeier, Pulsed-laser deposition of heteroepitaxial corundum-type ZITO: cor-In2−2xZnxSnxO3, Thin Solid Films 520 (2012) 2938–2942.
[15] C.A. Hoel, J.-F. Gaillard, K.R. Poeppelmeier, Probing the local structure of crystalline ZITO: In2−2xSnxZnxO3 (x≤0.4), J. Solid State Chem. 183 (2010) 761–768.
[16] P.P. Edwards, A. Porch, M.O. Jones, D.V. Morgan, R.M. Perks, Basic materials physics of transparent conducting oxides, Dalton Trans. 19 (2004) 2995–3002.
[17] J. Lee, S.-C. Lee, C.S. Hwang, J.-H. Choi, Thermodynamic stability of various phases of zinc tin oxides from ab initio calculations, J. Mater. Chem. C 1 (2013) 6364–6374.
[18] K. Nomura, H. Ohta, A. Takagi, T. Kamiya, M. Hirano, H. Hosono, Room-temperature fabrication of transparent flexible thin-film transistors using amorphous oxide semiconductors, Nature 432 (2004) 488–492.
[19] D.E. Proffit, D.B. Buchholz, R.P.H. Chang, M.J. Bedzyk, T.O. Mason, Q. Ma, X-ray absorption spectroscopy study of the local structures of crystalline Zn–In–Sn oxide thin films, J. Appl. Phys. 106 (2009) 113524.
[20] Y.-B. Lu, T.L. Yang, Z.C. Ling, W.-Y. Cong, P. Zhang, Y.H. Li, Y.Q. Xin, How does the multiple constituent affect the carrier generation and charge transport in multicomponent TCOs of In-Zn-Sn oxide, J. Mater. Chem. C 3 (2015) 7727–7737.
[21] Y.-B. Lu, Y.H. Li, Z.C. Ling, W.-Y. Cong, P. Zhang, Y.Q. Xin, T.L. Yang, Geometric, electronic and optical properties of zinc/tin codoped In 2 O 3 modulated by the bixbyite/corundum phase transition, J. Phys. D: Appl. Phys. 49 (2016) 065105.
[22] G. Hautier, A. Miglio, D. Waroquiers, G.-M. Rignanese, X. Gonze, How does chemistry influence electron effective mass in oxides? a high-throughput computational analysis, Chem. Mater. 26 (2014) 5447–5458.
[23] S.-J. Seo, C.G. Choi, Y.H. Hwang, B.-S. Bae, High performance solution-processed amorphous zinc tin oxide thin film transistor, J. Phys. D: Appl. Phys. 42 (2009) 035106.
[24] P.D.C. King, T.D. Veal, Conductivity in transparent oxide semiconductors, J. Phys.: Condens. Matter 23 (2011) 334214.
[25] D.E. Proffit, Q. Ma, D.B. Buchholz, R.P.H. Chang, M.J. Bedzyk, T.O. Mason, N.J. Dudney, Structural and physical property studies of amorphous Zn-In-Sn-O thin films, J. Am. Ceram. Soc. 95 (2012) 3657–3664.
[26] G.B. Palmer, K.R. Poeppelmeier, T.O. Mason, Conductivity and transparency of ZnO/SnO2-cosubstituted In2O3, Chem. Mater. 9 (1997) 3121–3126.
[27] G. Kresse, J. Furthmüller, Efficiency of ab-initio total energy calculations for metals and semiconductors using a plane-wave basis set, Comput. Mater. Sci. 6 (1996) 15–50.
[28] G. Kresse, J. Furthmüller, Efficient iterative schemes for ab initio total-energy calculations using a plane-wave basis set, Phys. Rev. B 54 (1996) 11169–11186.
[29] P.E. Blochl, Projector augmented-wave method, Phys. Rev. B 50 (1994) 17953–17979.
[30] G. Kresse, D. Joubert, From ultrasoft pseudopotentials to the projector augmented-wave method, Phys. Rev. B 59 (1999) 1758–1775.
[31] V.I. Anisimov, J. Zaanen, O.K. Andersen, Band theory and Mott insulators Hubbard U instead of Stoner I, Phys. Rev. B 44 (1991) 943–952.
[32] P. Erhart, A. Klein, R. Egdell, K. Albe, Band structure of indium oxide: Indirect versus direct band gap, Phys. Rev. B 75 (2007) 153205.
[33] H.-H. Nahm, Y.-S. Kim, Role of lone-pair electrons in Sb-doped amorphous InGaZnO4: Suppression of the hole-induced lattice instability, Appl. Phys. Lett. 102 (2013) 152101.
[34] Y.-B. Lu, Y. Dai, M. Guo, L. Yu, B.B. Huang, Investigation of magnetic properties induced by group-V element in doped ZnO, Phys. Chem. Chem. Phys. 15 (2013) 5208–5214.
[35] S.S. Farvid, T. Sabergharesou, L.N. Hutfluss, M. Hegde, E. Prouzet, P.V. Radovanovic, Evidence of charge-transfer ferromagnetism in transparent diluted magnetic oxide nanocrystals: switching the mechanism of magnetic interactions, J. Am. Chem. Soc. 136 (2014) 7669–7679.
[36] C.R. Stanek, K.J. McClellan, B.P. Uberuaga, K.E. Sickafus, M.R. Levy, R.W. Grimes, Determining the site preference of trivalent dopants in bixbyite sesquioxides by atomic-scale simulations, Phys. Rev. B 75 (2007) 134101.
[37] L. Bizo, J. Choisnet, R. Retoux, B. Raveau, The great potential of coupled substitutions in In2O3 for the generation of bixbyite-type transparent conducting oxides, In2−2xMxSnxO3, Solid State Commun. 136 (2005) 163–168.
[38] D.R. Kammler, T.O. Mason, K.R. Poeppelmeier, Bulk phase relations, conductivity, and transparency in novel bixbyite transparent conducting oxide solution in the cadmium-indium-tin oxide system, J. Am. Ceram. Soc. 84 (2001) 1004–1009.
[39] D.R. Kammler, T.O. Mason, K.R. Poeppelmeier, Phase relationships, transparency, and conductivity in the cadmium indate-cadmium stannate system, Chem. Mater. 12 (2000) 1954–1960.
[40] J. Ni, L. Wang, Y. Yang, H. Yan, S. Jin, T.J. Marks, J.R. Ireland, C.R. Kannewurf, Charge transport and optical properties of MOCVD-derived highly transparent and conductive Mg- and Sn-Doped In2O3 thin films, Inorg. Chem. 44 (2005) 6071–6076.
[41] D. Bérardan, E. Guilmeau, A. Maignan, B. Raveau, Enhancement of the thermoelectric performances of In[sub 2]O[sub 3] by the coupled substitution of M^{2+}/Sn^{4+} for In^{3+}, J. Appl. Phys. 104 (2008) 064918.
[42] A. Walsh, J.L.F. Da Silva, S.-H. Wei, Interplay between order and disorder in the high performance of amorphous transparent conducting oxides, Chem. Mater. 21 (2009) 5119–5124.
[43] C.A. Hoel, T.O. Mason, J.-F.O. Gaillard, K.R. Poeppelmeier, Transparent Conducting Oxides in the ZnO-In2O3-SnO2System, Chem. Mater. 22 (2010) 3569–3579.
[44] J.-Y. Noh, H. Kim, H.-H. Nahm, Y.-S. Kim, D. Hwan Kim, B.-D. Ahn, J.-H. Lim, G. Hee Kim, J.-H. Lee, J. Song, Cation composition effects on electronic structures of In-Sn-Zn-O amorphous semiconductors, J. Appl. Phys. 113 (2013) 183706.
[45] G. Trimarchi, H. Peng, J. Im, A.J. Freeman, V. Cloet, A. Raw, K.R. Poeppelmeier, K. Biswas, S. Lany, A. Zunger, Using design principles to systematically plan the synthesis of hole-conducting transparent oxides: Cu_3VO_4 and Ag_3VO_4 as a case study, Phys. Rev. B 84 (2011) 165116.
[46] J.E. Medvedeva, C.L. Hettiarachchi, Tuning the properties of complex transparent conducting oxides: role of crystal symmetry, chemical composition, and carrier generation, Phys. Rev. B 81 (2010) 125116.